

# Co-RaL: Complementary Radar-Leg Odometry with 4-DoF Optimization and Rolling Contact

Sangwoo Jung<sup>1</sup>, Wooseong Yang<sup>1</sup>, and Ayoung Kim<sup>1\*</sup>

**Abstract**— Robust and accurate localization in challenging environments is becoming crucial for SLAM. In this paper, we propose a unique sensor configuration for precise and robust odometry by integrating chip radar and a legged robot. Specifically, we introduce a tightly coupled radar-leg odometry algorithm for complementary drift correction. Adopting the 4-DoF optimization and decoupled RANSAC to mmWave chip radar significantly enhances radar odometry beyond the existing method, especially z-directional even when using a single radar. For the leg odometry, we employ rolling contact modeling-aided forward kinematics, accommodating scenarios with the potential possibility of contact drift and radar failure. We evaluate our method by comparing it with other chip radar odometry algorithms using real-world datasets with diverse environments while the datasets will be released for the robotics community. <https://github.com/SangwooJung98/Co-RaL-Dataset>

## I. INTRODUCTION

Attaining precise and robust odometry in extreme environments is receiving a prominent focus [1–5]. Navigating such environments demands robust perception and agile mobility. Providing such dexterous mobility, legged robots have emerged recently due to their compatibility in unstructured environments. For most legged robots, common practice is to equip the legged robot with cameras and Light Detection and Ranging (LiDAR) for their extrovert perception. However, these perceptual sensors are susceptible to visual degradation and feature degeneration, leading to sensor potential failures. Being a robust perceptual sensor in extreme environments, radar can be a promising solution but mainly applied to unmanned ground vehicle (UGV)s and drones, not to the legged robots. This paper presents a tightly coupled radar-leg odometry, validating the enhanced odometry performance from their complementary nature.

Radar stands out as a widely utilized range sensor in robotics, renowned for its robustness in extreme environmental conditions such as rain, dust, or snow. Furthermore, Frequency Modulated Continuous Wave (FMCW) technique enables the radar to gather the radial velocity of points included in the point cloud, which may exploited for noise or small dynamic object reduction and ego-velocity calculation [6]. However, challenges arise from the sparse point cloud and low elevation accuracy, leading to potential vertical drift in estimating odometry as Fig. 1.

Legged robots, in contrast to traditional wheeled UGV, show superior adaptability to varied terrains, including chal-

<sup>†</sup>This work was supported by the MOTIE (1415187329) and MSIT (No.2022-0-00480).

<sup>1</sup>S. Jung, W. Yang, and A. Kim are with the Department of Mechanical Engineering, SNU, Seoul, S. Korea [dan0130, yellowish, ayoungk]@snu.ac.kr

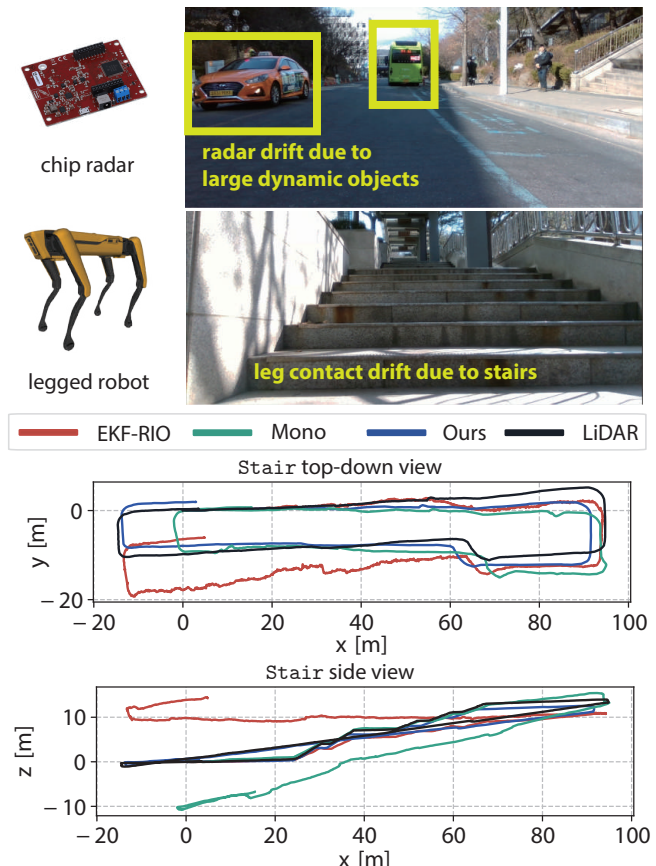


**Fig. 1:** Example of radar drift scene that includes large dynamic objects and leg contact drift scene including frequent contact impact and vibration. Large dynamic objects are shown in the yellow box. Both scenes are recorded using the intel realsense D435i attached to the SPOT sensor system while acquiring Stair sequence. Odometry of the proposed method (Ours) and comparison group are included in top-down and side views.

lenging environments like fire sites, mountain trails, and stairs, due to their reduced dependence on ground structure. These robots leverage contact sensors and joint encoders to compute odometry. The estimated velocity from legged robots is not influenced by dynamic objects and offers accurate z-axis information, thanks to forward kinematics. Nonetheless, variations in ground conditions can lead to contact slip or drift, which may compromise the reliability of leg measurements. To address this, the integration of cameras and LiDARs has been proposed to enhance leg odometry robustness with external sensors [7]. However, it's crucial to note that the advantages offered by cameras and LiDARs might be mitigated in extreme conditions—environments where legged robots typically excel—due to the suscepti-

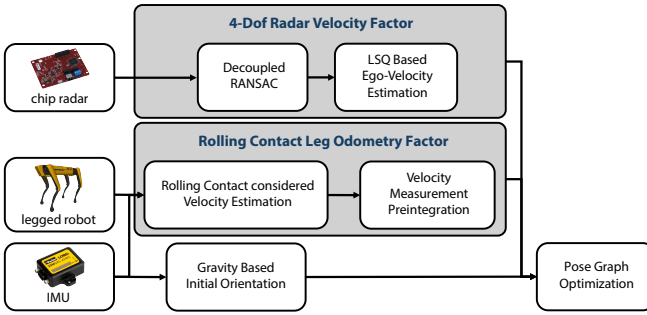


**Fig. 2:** Pipeline of the proposed system with 4-DoF radar velocity factor and rolling contact preintegrated leg odometry factor.

bility of these sensors to such challenging scenarios.

To the best of our knowledge, our system is the first integration of radar and leg for ego-motion estimation. We introduce a tightly integrated radar-leg odometry designed to mutually correct drifts (Fig. 2). By transforming the challenge into a 4-degree of freedom (DoF) problem and employing random sample consensus (RANSAC) on two decoupled planes, we enhance radar odometry beyond the existing methods even with using a single radar. Additionally, we account for the rolling-contact modeling in leg odometry, accommodating scenarios such as stair navigation. Our contributions can be summarized as follows:

- **Substantial z-directional accuracy improvement** We are the first to apply the 4-DoF optimization scheme to radar, which is widely leveraged on the vision group [8, 9]. Additionally, we introduce decoupled RANSAC specifically for z-directional outlier removal. Proposed method substantially improves the radar odometry in the z-direction, even using a single-chip radar.
- **Rolling contact for preintegrated leg odometry** This paper handles the rolling contact movement of the contact surface by including the rolling motion on the contact surface to the body velocity derivation, the velocity measurement model with less bias is achieved.
- **Thorough real-world evaluation** Using a real-world radar-leg dataset, we evaluate the proposed method by comparing it against other existing algorithms. Our method shows substantially improved accuracy and robustness, especially in the z-axis translation. We will release the dataset for this unique sensor combination to boost the research in this field.

## II. RELATED WORK

### A. mmWave Chip Radar Odometry

Using radar for ego-motion estimation has been introduced in various ways. Kellner et al. [6] proposed an instantaneous ego-motion estimation using a single-chip radar, which was later extended to multiple chip radars [10]. Doer and Trommer [11] proposed an extended Kalman Filter (EKF) based fusion between chip radar and inertial measurement unit (IMU) while exploiting the ego velocity estimation solution of [6]. Park et al. [12] estimated 3D ego-velocity in a similar manner of [10] by exploiting two perpendicular chip radar systems while proposing a radar velocity factor for

pose graph simultaneous localization and mapping (SLAM) that leverages rotation information from IMU. Unfortunately, even when using multiple radars, inaccurate elevation due to precision of the chip radar and the inability to resolve drift caused by large dynamic objects still remain.

Recent works focus on leveraging the radar pointcloud at the point level to include spatial information on the resulting trajectory. Michalczyk et al. [13] proposed exploiting stochastic cloning to match 3D points on consecutive pointclouds. Zhuang et al. presented 4D-iRIOM [14] that fuses ego-velocity and scan matching. By combining sensitive but accurate scan-to-submap registration with robust ego-velocity, 4D-iRIOM [14] achieved accurate odometry of the UGV. Leveraging ground point characteristics has been done on DRIO [15]. By simultaneously estimating the radar velocity and detecting ground points, DRIO [15] accomplished robust 3D odometry. Recently, Huang et al. [16] exploited the Radar Cross Section (RCS)-bounded filter to refine point-to-point correspondences. More recently, the deep learning was considered to handle the high-level noise [17]. Yet, due to its noise and sparseness, potential failure of optimization and environmental constraints should be further resolved.

We present a single-chip radar factor that is more robust on vertical drift compared with [11, 12], leveraging elevation noise removal and 4-DoF optimization. Compared to the existing methods, ours yields improvement in z-directional error, which mutually compensates with leg odometry.

### B. Legged Robot Odometry

Being the major sensor in a legged robot, contact sensor provides information about whether the robot's foot is contacting the ground. Hartley et al. [18] proposed forward kinematics factor and preintegrated contact factor for the graph optimization. Later, [19] expands [18] in the manner of hybrid contact theory that the contact frame may switch while integration as at least one foot is contacting on the ground. Based on the contact theory, Hartley et al. proposed [20] that included the contact kinematics theory with the invariant EKF model to integrate it with other exteroceptive sensors. Though the contact frames may provide reliable landmarks to the robot based on the forward kinematics, contact drift or slip may occur movement on the contact frame, which accumulates the error on robot pose.

Calculating robot velocity based on the differential of forward kinematics from the contact frame to the robot frame is one method of exploiting the joint encoder and contact sensor as a proprioceptive odometry sensor. Wisth et al. [21] proposed a preintegrated velocity factor that includes bias estimation to overcome contact nonlinearities, being fused with the camera to calculate odometry. VILENS [7] extended the previous work [21] by tightly fusing camera, LiDAR, IMU, and preintegrated leg factor from [21] to achieve robust odometry that can be exploited on feature degenerate, low light, and even deformable ground environment.

Inspired by VILENS [7], we conduct a preintegrated velocity factor exploiting the joint encoder and contact sensor. Differing from them, we consider the rolling contact of

the contact frame. Separating the portion of velocity bias occurring from the rolling contact may lower the burden of optimizing velocity bias in the optimization process.

### III. 4-DOF RADAR VELOCITY FACTOR

#### A. Decoupled RANSAC for Outlier Rejection

Pointcloud from chip radar provides the radial velocity of each point, but a high level of noise and inaccurate elevation information problems exist. In this section, we introduce our two-staged outlier removal.

1) *xy Plane Outlier Removal*: Similar to [6, 10, 12], the initial RANSAC process removes small dynamic objects and noise from the pointcloud. After the *xy* plane projection, the point position is changed into a polar coordinate system, changing into  $(r_{xy}, \theta_{xy})$ . If a point is generated from a static object, 2D radial velocity  $v_{xy}$  should be the same as the robot velocity of point direction  $\theta_{xy}$ , which follows a sinusoidal curve [10]. Based on the sinusoidal curve fitting, the 2D velocity of robot  $(v_x, v_y)$  and static points are extracted.

2) *z-directional Outlier Removal*: The extracted inlier pointcloud data with noise and dynamic objects removed may include the remaining inaccuracy in the z-axis position.

The follow-up RANSAC starts with projecting these filtered inlier points to the *xz* plane. Every position information of projected points  $(x, z)$  is changed into a polar coordinate  $(r_{xz}, \theta_{xz})$ . For that point whose z-axis information is accurate,  $\theta_{xz}$  and  $r_{xz}$  should follow the sinusoidal curve.

The x-axis velocity  $v_x$  calculated from the previous phase is reliable since it only exploits the  $v_{xy}$  of the static points. Therefore, fixing the  $v_x$  may enhance the performance of RANSAC fitting to remove the points whose elevation is inaccurate. After removing outliers, Least Square (LSQ) optimization computes the 3D ego-velocity as  $\hat{\mathbf{v}} = [\hat{v}_x \hat{v}_y \hat{v}_z]^\top$ .

#### B. 4-DoF Radar Velocity Factor

Visual and LiDAR SLAM works as [8, 9] has exploited the characteristic that the direction of gravity vector is constant to optimize only  $x, y, z$ , and yaw to enhance the optimization accuracy, especially on the z-axis. In this work, we decouple the orientation state of the 6-DoF radar factor from [12] into roll, pitch, and yaw. After decoupling, we fix the roll and pitch values as the initial measurements of IMU to prevent inaccurate optimization. Derivation in this paper only includes the residual function and Jacobian matrix to highlight the parts different from [12].

Residual error included in [12] are as follows:

$$\begin{aligned} \mathbf{r}_{\Delta p_{ij}} &= \mathbf{R}_i^\top (\mathbf{p}_j - \mathbf{p}_i - \mathbf{v}_i \Delta t) \\ &\quad - \left[ \Delta \tilde{\mathbf{p}}_{ij} (\bar{\mathbf{b}}_j^r) + \frac{\partial \Delta \bar{\mathbf{p}}_{ij}}{\partial \mathbf{b}^r} \delta \mathbf{b}_j^r \right] \end{aligned} \quad (1)$$

$$\mathbf{r}_{\mathbf{v}_j} = \mathbf{v}_j - \left[ \tilde{\mathbf{v}}_j (\bar{\mathbf{b}}_j^r) + \frac{\partial \tilde{\mathbf{v}}_j}{\partial \mathbf{b}^r} \delta \mathbf{b}_j^r \right] \quad (2)$$

$$\|\mathbf{r}_{\Delta b_{ij}^r}\|^2 = \|\mathbf{b}_j^r - \bar{\mathbf{b}}_j^r\|^2 \quad (3)$$

, while  $\mathbf{R}_i$ ,  $\mathbf{p}_i$ ,  $\mathbf{v}_i$ ,  $\mathbf{b}_i^r$  are the orientation, position, velocity, and radar velocity bias at state  $i$ . By dividing orientation state into roll, pitch, and yaw,  $\mathbf{R}_i$  changes into  $\mathbf{R}(\gamma_i)\mathbf{R}(\beta_i)\mathbf{R}(\alpha_i)$

when the  $\alpha, \beta, \gamma$  are roll, pitch, yaw of  $\mathbf{R}_i$  and  $\mathbf{R}()$  is  $\text{Exp}([\alpha \ 0 \ 0]^\top \times)$ ,  $\text{Exp}([0 \ \beta \ 0]^\top \times)$ ,  $\text{Exp}([0 \ 0 \ \gamma]^\top \times)$  for roll, pitch, yaw each.  $\text{Exp}()$  and  $\text{Log}()$  an exponential mapping and logarithm mapping in Lie algebra, while  $\mathbf{v}_\times$  is a skew matrix of the vector  $\mathbf{v}$ . As  $\mathbf{r}_{\mathbf{v}_j}$  and  $\|\mathbf{r}_{\Delta b_{ij}^r}\|^2$  are not including  $\mathbf{R}_i$ , only  $\mathbf{r}_{\Delta p_{ij}}$  changes:

$$\begin{aligned} \mathbf{r}_{\Delta p_{ij}} &= \mathbf{R}(\alpha_i)^\top \mathbf{R}(\beta_i)^\top \mathbf{R}(\gamma_i)^\top (\mathbf{p}_j - \mathbf{p}_i - \mathbf{v}_i \Delta t) \\ &\quad - \left[ \Delta \tilde{\mathbf{p}}_{ij} (\bar{\mathbf{b}}_j^r) + \frac{\partial \Delta \bar{\mathbf{p}}_{ij}}{\partial \mathbf{b}^r} \delta \mathbf{b}_j^r \right] \end{aligned} \quad (4)$$

Similarly, orientation state  $\mathbf{R}_i$  is changed into  $\alpha_i, \beta_i, \gamma_i$  state.

For the Jacobian, perturbation for  $\gamma_i$  is only performed as the roll and pitch values are not optimized. To simplify the notion using perturbation,  $\delta \gamma_i^{\text{vec}} = [0 \ 0 \ \delta \gamma_i]^\top$  Using the first-order approximation of the exponential map, the Jacobian of  $\mathbf{r}_{\Delta p_{ij}}$  about  $\gamma_i$  is derived as follows by starting with changing  $\gamma_i$  in  $\mathbf{r}_{\Delta p_{ij}}$  into  $\gamma_i + \delta \gamma_i$ :

$$\begin{aligned} \mathbf{r}'_{\Delta p_{ij}} &= \mathbf{R}(\alpha_i)^\top \mathbf{R}(\beta_i)^\top \mathbf{R}(\gamma_i + \delta \gamma_i^{\text{vec}})^\top (\mathbf{p}_j - \mathbf{p}_i - \mathbf{v}_i \Delta t) \\ &\quad - \left[ \Delta \tilde{\mathbf{p}}_{ij} (\bar{\mathbf{b}}_j^r) + \frac{\partial \Delta \bar{\mathbf{p}}_{ij}}{\partial \mathbf{b}^r} \delta \mathbf{b}_j^r \right] \end{aligned} \quad (5)$$

$$\begin{aligned} &= \mathbf{R}(\alpha_i)^\top \mathbf{R}(\beta_i)^\top \left( \mathbf{I} - \delta \gamma_i^{\text{vec}} \times \right) \mathbf{R}(\gamma_i)^\top (\mathbf{p}_j - \mathbf{p}_i - \mathbf{v}_i \Delta t) \\ &\quad - \left[ \Delta \tilde{\mathbf{p}}_{ij} (\bar{\mathbf{b}}_j^r) + \frac{\partial \Delta \bar{\mathbf{p}}_{ij}}{\partial \mathbf{b}^r} \delta \mathbf{b}_j^r \right] \end{aligned} \quad (6)$$

$$\begin{aligned} &= \mathbf{R}(\alpha_i)^\top \mathbf{R}(\beta_i)^\top \left( \mathbf{R}(\gamma_i)^\top (\mathbf{p}_j - \mathbf{p}_i - \mathbf{v}_i \Delta t) \right)_\times \delta \gamma_i^{\text{vec}} \\ &\quad + \mathbf{r}_{\Delta p_{ij}} \end{aligned} \quad (7)$$

Furthermore, as the  $\delta \gamma_i^{\text{vec}} = [0 \ 0 \ \delta \gamma_i]^\top$ ,

$$\text{let } \frac{\partial \mathbf{r}_{\Delta p_{ij}}}{\partial \phi_i} = \begin{bmatrix} a & b & c \\ d & e & f \\ g & h & i \end{bmatrix}, \text{ then } \frac{\partial \mathbf{r}_{\Delta p_{ij}}}{\partial \gamma_i} = \begin{bmatrix} c \\ f \\ i \end{bmatrix} \quad (8)$$

(Third column of  $\mathbf{R}(\alpha_i)^\top \mathbf{R}(\beta_i)^\top \left( \mathbf{R}(\gamma_i)^\top (\mathbf{p}_j - \mathbf{p}_i - \mathbf{v}_i \Delta t) \right)_\times$ )

Based on the derivation of  $\frac{\partial \mathbf{r}_{\Delta p_{ij}}}{\partial \gamma_i}$ , the Jacobian of the  $\alpha_i, \beta_i, \gamma_i$  is as (9) while most of the matrix is filled with zero due to the 4-DoF optimization and blank area is same as (8), which is not intuitive to write with its components due to its formula.

$$\begin{aligned} &\left[ \begin{array}{c|ccccc} \frac{\partial \mathbf{r}_{\Delta p_{ij}}}{\partial \alpha_i} & \frac{\partial \mathbf{r}_{\Delta p_{ij}}}{\partial \beta_i} & \frac{\partial \mathbf{r}_{\Delta p_{ij}}}{\partial \gamma_i} & \frac{\partial \mathbf{r}_{\Delta p_{ij}}}{\partial \alpha_j} & \frac{\partial \mathbf{r}_{\Delta p_{ij}}}{\partial \beta_j} & \frac{\partial \mathbf{r}_{\Delta p_{ij}}}{\partial \gamma_j} \\ \hline \frac{\partial \mathbf{r}_{\Delta p_{ij}}}{\partial \phi_i} & \frac{\partial \mathbf{r}_{\Delta p_{ij}}}{\partial \mathbf{r}_j} & \frac{\partial \mathbf{r}_{\Delta p_{ij}}}{\partial \mathbf{v}_j} & \frac{\partial \mathbf{r}_{\Delta p_{ij}}}{\partial \Delta \mathbf{b}_{ij}^r} & \frac{\partial \mathbf{r}_{\Delta p_{ij}}}{\partial \Delta \mathbf{b}_{ij}^r} & \frac{\partial \mathbf{r}_{\Delta p_{ij}}}{\partial \Delta \mathbf{b}_{ij}^r} \\ \hline \frac{\partial \mathbf{r}_{\Delta p_{ij}}}{\partial \alpha_i} & \frac{\partial \mathbf{r}_{\Delta p_{ij}}}{\partial \beta_i} & \frac{\partial \mathbf{r}_{\Delta p_{ij}}}{\partial \gamma_i} & \frac{\partial \mathbf{r}_{\Delta p_{ij}}}{\partial \Delta \mathbf{b}_{ij}^r} & \frac{\partial \mathbf{r}_{\Delta p_{ij}}}{\partial \Delta \mathbf{b}_{ij}^r} & \frac{\partial \mathbf{r}_{\Delta p_{ij}}}{\partial \Delta \mathbf{b}_{ij}^r} \end{array} \right] \\ &= \left[ \begin{array}{ccc|ccc} \mathbf{0}_{3 \times 1} & \mathbf{0}_{3 \times 1} & - & \mathbf{0}_{3 \times 1} & \mathbf{0}_{3 \times 1} & \mathbf{0}_{3 \times 1} \\ \mathbf{0}_{3 \times 1} & \mathbf{0}_{3 \times 1} \\ \mathbf{0}_{3 \times 1} & \mathbf{0}_{3 \times 1} \end{array} \right] \end{aligned} \quad (9)$$

(9) is the altered orientation part of the residual Jacobian from the original 6-DoF radar factor [12].

### IV. ROLLING CONTACT LEG ODOMETRY FACTOR

This section is divided into two subsections. Firstly, we include velocity estimation using kinematic information and rolling contact assumption. Then we apply the preintegrated leg odometry factor introduced from [7] to the estimated velocity. Unlike the previous radar section, the derivation is more concentrated between “frames” not “time”,  $i$  that marks the state  $i$  is omitted in the following derivation.

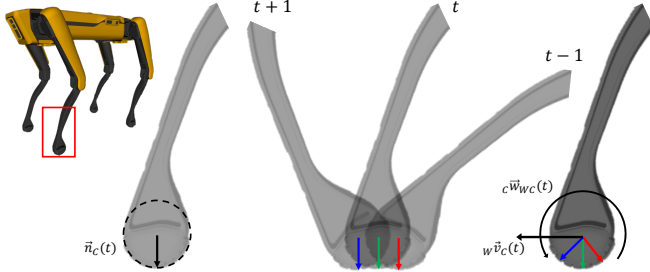


**Fig. 3:** Overview of the rolling contact on legged robots with round feet. Rolling motion on the contact frame occurs as the robot moves.

#### A. Kinematic Velocity Estimation with Rolling Contact

Prior to the derivation of robot base velocity, the relationship between the body-contact frame and forward kinematic functions is defined as follows:

$$\mathbf{R}_{BC} = \mathbf{f}_R(\alpha) \quad (10)$$

$$\mathbf{b}\dot{\mathbf{p}}_C = \mathbf{f}_p(\alpha) \quad (11)$$

where the  $\alpha$  is the measured joint angle and  $\mathbf{f}_R$ ,  $\mathbf{f}_p$  are forward kinematic functions about orientation and translation between robot body frame and contact frame each. Both (10) and (11) are differentiated with the Jacobians of each forward kinematic function as follows.

$$\dot{\mathbf{R}}_{BC} = \mathbf{R}_{BC} \mathbf{c}\omega_{BC}^\wedge = \mathbf{J}_R(\alpha, \dot{\alpha}) \quad (12)$$

$$\mathbf{b}\dot{\mathbf{p}}_C = \mathbf{b}\mathbf{v}_C = \mathbf{J}_p(\alpha, \dot{\alpha}) \quad (13)$$

Robot base velocity derivation begins from the relationship between the contact and world frames.

$$\mathbf{R}_{WC} = \mathbf{R}_{WB} \mathbf{R}_{BC} \quad (14)$$

$$\mathbf{w}\mathbf{p}_C = \mathbf{w}\mathbf{p}_B + \mathbf{R}_{WB} \mathbf{b}\mathbf{p}_C \quad (15)$$

Most of the previous works that calculated robot velocity based on the contact kinematics started with the assumption that  $\mathbf{R}_{WC}$  and  $\mathbf{w}\mathbf{p}_C$  are zero matrix or zero vector as the contact frame is fixed on the ground [7]. Following the rolling contact assumption as Fig. 3, we included the movement of the contact frame with respect to the world frame in the derivation process. By differentiating (14), the skew matrix of the robot base frame's angular velocity with respect to the world frame is derived as follows:

$$\dot{\mathbf{R}}_{WC} = \dot{\mathbf{R}}_{WB} \mathbf{R}_{BC} + \mathbf{R}_{WB} \dot{\mathbf{R}}_{BC} \quad (16)$$

$$= \mathbf{R}_{WB} \mathbf{b}\omega_{WB}^\wedge \mathbf{R}_{BC} + \mathbf{R}_{WB} \mathbf{R}_{BC} \mathbf{c}\omega_{BC}^\wedge \\ = \mathbf{R}_{WC} \mathbf{c}\omega_{WC}^\wedge = \mathbf{R}_{WB} \mathbf{R}_{BC} \mathbf{c}\omega_{WC}^\wedge$$

$$\mathbf{R}_{BC} \mathbf{c}\omega_{WC}^\wedge = \mathbf{b}\omega_{WB}^\wedge \mathbf{R}_{BC} + \mathbf{R}_{BC} \mathbf{c}\omega_{BC}^\wedge \quad (17)$$

$$\mathbf{b}\omega_{WB}^\wedge = \mathbf{R}_{BC} \mathbf{c}\omega_{WC}^\wedge \mathbf{R}_{CB} - \mathbf{R}_{BC} \mathbf{c}\omega_{BC}^\wedge \mathbf{R}_{CB} \quad (18)$$

As the rolling motion of the contact frame follows the movement of Fig. 3, the skew matrix of the contact frame's angular velocity with respect to the world frame is derived as follows by exploiting the orientation of the contact frame:

$$\mathbf{R}_{WC}^t = \mathbf{R}_{WC}^{t-1} \text{Exp}(\mathbf{c}\omega_{WC}^\wedge(t) \Delta t) \quad (19)$$

$$\mathbf{c}\omega_{WC}^\wedge(t) = \frac{1}{\Delta t} \text{Log}(\mathbf{R}_{CW}^{t-1} \mathbf{R}_{WC}^t) \quad (20)$$

while the orientation of the contact frame is calculated with IMU orientation and forward kinematic function. Substituting the  $\mathbf{c}\omega_{WC}^\wedge$  and rotation matrixes in (18) with forward kinematics functions,  $\mathbf{b}\omega_{WB}^\wedge$  is derived as follow:

$$\therefore \mathbf{b}\omega_{WB}^\wedge = \mathbf{f}_R(\alpha) \frac{1}{\Delta t} \text{Log}(\mathbf{R}_{CW}^{t-1} \mathbf{R}_{WC}^t) (\mathbf{f}_R(\alpha))^\top \quad (21) \\ - \mathbf{J}_R(\alpha, \dot{\alpha}) (\mathbf{f}_R(\alpha))^\top$$

Linear velocity  $\mathbf{w}\mathbf{v}_B$  is achieved by differentiating the (15).

$$\mathbf{w}\dot{\mathbf{p}}_C = \mathbf{w}\dot{\mathbf{p}}_B + \dot{\mathbf{R}}_{WB} \mathbf{b}\mathbf{p}_C + \mathbf{R}_{WB} \mathbf{b}\dot{\mathbf{p}}_C \quad (22)$$

$$\mathbf{w}\mathbf{v}_B = -\mathbf{R}_{WB} \mathbf{b}\omega_{WB}^\wedge \mathbf{b}\mathbf{p}_C - \mathbf{R}_{WB} \mathbf{b}\dot{\mathbf{p}}_C + \mathbf{w}\dot{\mathbf{p}}_C \quad (23)$$

$$= -\mathbf{R}_{WB} \mathbf{b}\omega_{WB}^\wedge \mathbf{f}_p(\alpha) - \mathbf{R}_{WB} \mathbf{J}_p(\alpha, \dot{\alpha}) + \mathbf{w}\dot{\mathbf{p}}_C$$

Due to the rolling contact assumption, the linear velocity of the contact frame with respect to the world frame is calculated using the normal vector from ground to contact frame as Fig. 3:  $\mathbf{w}\dot{\mathbf{p}}_C = \mathbf{n}_C \times \mathbf{c}\omega_{WC} = -\mathbf{c}\omega_{WC}^\wedge \mathbf{n}_C$ . Finally, 6-DoF velocity of the robot base in world frame is derived :

$$\mathbf{b}\omega_{WB}^\wedge = \mathbf{f}_R(\alpha) \frac{1}{\Delta t} \text{Log}(\mathbf{R}_{CW}^{t-1} \mathbf{R}_{WC}^t) (\mathbf{f}_R(\alpha))^\top \quad (24) \\ - \mathbf{J}_R(\alpha, \dot{\alpha}) (\mathbf{f}_R(\alpha))^\top$$

$$\mathbf{w}\mathbf{v}_B = -\mathbf{R}_{WB} \mathbf{b}\omega_{WB}^\wedge \mathbf{f}_p(\alpha) - \mathbf{R}_{WB} \mathbf{J}_p(\alpha, \dot{\alpha}) \quad (25) \\ - \mathbf{c}\omega_{WC}^\wedge \mathbf{n}_C$$

#### B. Preintegrated Leg Odometry Factor

We apply the rolling contact considered velocity measurement to the preintegrated odometry factor.

1) *Velocity Bias:* Though the rolling contact assumption may handle a portion of the bias on robot velocity, contact drift that may occur due to the slippery or deformable terrain still remains. In this manner, we tenant the slowly varying bias term  $\mathbf{b}^l$  [7] to robot body velocity (25) as

$$\tilde{\mathbf{v}} = \mathbf{v} + \mathbf{b}^l + \boldsymbol{\eta}^v \quad (26)$$

with the white noise  $\boldsymbol{\eta}^v$  based on zero-mean Gaussian.

2) *Velocity Measurements Preintegration:* As the measured velocity from IV-A is the linear velocity of the robot body with respect to the world frame, position at time  $t_j = t_i + \Delta t$  is

$$\mathbf{p}_j = \mathbf{p}_i + \int_{t_i}^{t_j} \mathbf{v}(\tau) d\tau \\ = \mathbf{p}_i + \sum_{k=i}^{j-1} [(\tilde{\mathbf{v}}_k - \mathbf{b}^l_k - \boldsymbol{\eta}^v_k) \Delta t] \quad (27)$$

Relative measurement and noise separation are as follows:

$$\Delta \mathbf{p}_{ij} = \sum_{k=i}^{j-1} [(\tilde{\mathbf{v}}_k - \mathbf{b}^l_k - \boldsymbol{\eta}^v_k) \Delta t] \\ = \Delta \tilde{\mathbf{p}}_{ij} - \delta \mathbf{p}_{ij} \quad (28)$$

$$\Delta \tilde{\mathbf{p}}_{ij} = \sum_{k=i}^{j-1} [(\tilde{\mathbf{v}}_k - \mathbf{b}^l_k) \Delta t] \quad (29)$$

$$\delta \mathbf{p}_{ij} = \sum_{k=i}^{j-1} [\boldsymbol{\eta}^v_k \Delta t] \quad (30)$$

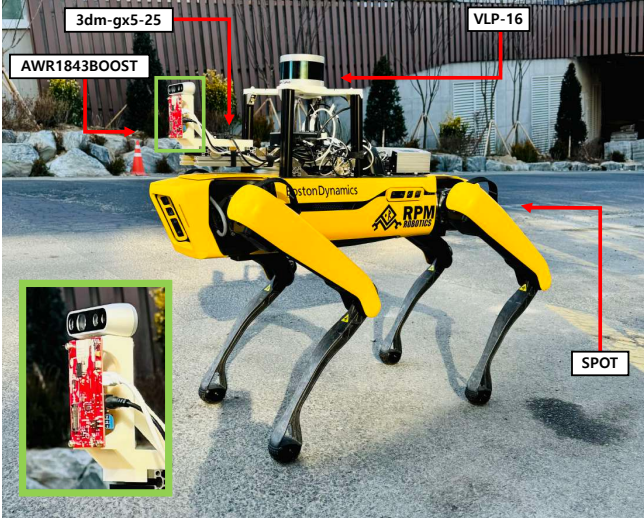


**Fig. 4:** System configuration. LiDAR and camera are attached only for baseline trajectory generation and video recording.

while  $\Delta\tilde{\mathbf{p}}_{ij}$  depends on the slowly varying bias  $\mathbf{b}^l$ . To avoid the recomputation of  $\Delta\tilde{\mathbf{p}}_{ij}$  for every input, we exploit the first order approximation as  $\mathbf{b} = \bar{\mathbf{b}} + \delta\mathbf{b}$  following [22].

$$\Delta\tilde{\mathbf{p}}_{ij}(\mathbf{b}^l) \simeq \Delta\tilde{\mathbf{p}}_{ij}(\bar{\mathbf{b}}^l) + \frac{\partial\tilde{\mathbf{p}}_{ij}}{\partial\mathbf{b}^l}\delta\mathbf{b} \quad (31)$$

**3) Residual:** The preintegrated velocity factor residual only includes the translation to give more focus on the effect of 4-DoF optimization from section III.

$$\mathbf{r}_{\Delta\mathbf{p}_{ij}} = \mathbf{p}_j - \mathbf{p}_i - \Delta\tilde{\mathbf{p}}_{ij}(\mathbf{b}^l) \quad (32)$$

## V. EXPERIMENTS

### A. Experiment Setup

The system configuration for experiments is shown in Fig. 4. We built our sensor system on the SPOT from Boston Dynamics, a legged UGV that can provide joint encoder and contact sensor data at 180 Hz. The AWR1843BOOST radar, which acquires 4D radar pointcloud for 20 Hz, and the 3dm-gx5-25 IMU from Microstrain working with 100 Hz are exploited. Finally, VLP-16 LiDAR operating in 10 Hz is mounted to generate baseline trajectory.

**1) Comparison Targets:** We compare the proposed method (Ours) against the following five methods.

- **FAST-LIO2:** FAST-LIO2 [23] is utilized to calculate a baseline trajectory (LiDAR).
- **6-DoF Mono:** Original radar factor of [12] that is working with single radar and 6-DoF optimization (Mono).
- **EKF-RIO:** Best performing open-sourced chip radar odometry method known to us [11] (EKF-RIO).
- **Leg only:** We only use the preintegrated leg factor to optimize the robot pose for comparison (Leg).
- **Radar only:** We only use the 4-DoF radar factor to optimize the robot pose for comparison (Radar).
- **Proposed method:** Our method includes both preintegrated leg factor and 4-DoF radar factor (Ours).

**2) Dataset:** To evaluate our proposed method, we acquired datasets covering a total of 1.2 km for 24 min in various environments such as stairs, slopes, wide and narrow passages, indoors and outdoors, and elevation changes. A brief introduction to dataset sequences is as follows:

- **Stair:** **Stairs that connects the buildings.** Start in front of the building, go up the stairs about 15 m, and return to the original position following a slope.
- **Under:** **Underground parking lot.** Start from B1, down to B2, and go around the floor. Return to the original location at B1.
- **Narrow:** **Walking trails inside university.** Start in front of the building, pass between narrow partitions only a single person can pass through, then walk around the wide space and return to the original position.
- **Trail:** **Mountain trail in university.** Start in front of the building and go straight up to the mountain trail; after going up 11 m, return to the original location.
- **Garage:** **Garage with narrow corridor and outside of the building.** Start from the garage. Go through the corridor and move along the outer wall of the building, returning to the initial location inside the garage.
- **Building:** **Inside and outside of the building.** Start moving outside of the building. Move along the slope and get through the underground passage. Climb the stairs about 8 m and return to the original position.

Table I includes more detailed information about the dataset.

### B. Quantitative Result

We calculated the root mean square error (RMSE) of the Absolute Trajectory Error (ATE) and Relative Trajectory Error (RTE) using rpg-trajectory evaluator [24] as the evaluation metric. Additionally, we added ATE for the z-axis as a sub-metric to evaluate the performance of the algorithms more focusing on vertical drift. ATE<sub>t</sub>, RTE<sub>t</sub>, and ATE<sub>z</sub> are measured in meters and ATE<sub>r</sub>, RTE<sub>r</sub> are measured in degrees. Quantitative results are summarized in Table. II while top-down view and side view plots are included in Fig. 5. Compared with the EKF-RIO and Mono, the proposing factors provide higher accuracy odometry on most sequences, especially in the z-axis. A more detailed analysis is provided in the attached video.

### C. Radar Drift Reduction by Leg Factor

Combining leg odometry with a radar sensor reduces odometry drift that may occur due to the occlusion of large dynamic objects(e.g., buses and cars as in Fig. 1). In Fig. 5(a), Fig. 5(b), and Fig. 5(i), it can be found that drift has occurred on Radar trajectory which is caused by the cars and pedestrians passing at close range. Nevertheless, Ours trajectory showed robustness on drift by tightly fusing radar and leg. Furthermore, though the consecutive drift has occurred on Trail sequence as it can be found from Fig. 5(g), Ours estimated reasonable odometry, more relying on the information from kinematic sensors. By fusing leg odometry factor with radar factor, Ours generated robust odometry to radar velocity drift.

**TABLE I:** Dataset description

Sequence	Environment	Stair	Slope	Narrow Path	Path Length (m)	Elevation Change (m)	Duration (s)	Avg. vel. (m/s)
Stair	Outdoor	✓	✓	✗	253.24	15.12	304.40	0.832
Under	Indoor	✗	✓	✗	227.02	3.23	258.50	0.878
Narrow	Outdoor	✗	✗	✓	134.86	-	151.39	0.891
Trail	Outdoor	✗	✓	✗	230.10	11.37	253.36	0.908
Garage	Hybrid	✗	✗	✓	138.52	-	161.68	0.857
Building	Hybrid	✓	✓	✗	252.86	8.26	291.89	0.866

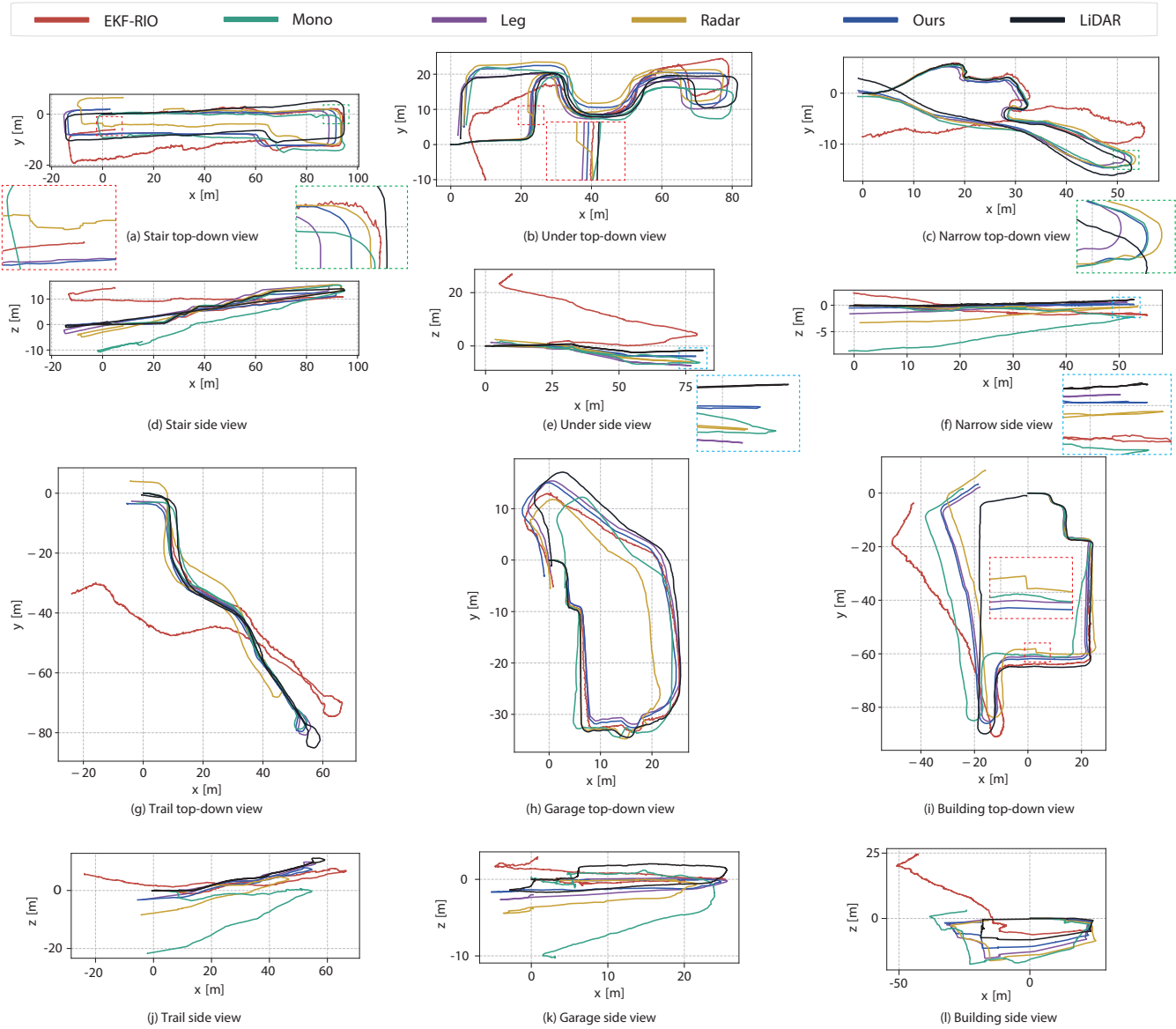


**Fig. 5:** Trajectory result of each sequence's top-down and side views. Color matching of methods is the same for every graph. The red, green, and blue dotted boxes and their enlarged figures are for V-C, V-D, and V-E, respectively.

#### D. Leg Velocity Scale Handling by Radar Factor

Though the leg odometry may show robustness and stability in every dataset, due to the contact impact that occurs at every step, inevitable contact drift may not be solved with rolling contact assumption and bias term. This leads to the leg velocity scale issue, making Leg trajectory reduced, compared to the LiDAR trajectory. However, the radar sensor is free from the scale issue of the leg factor, which can be

found in Fig. 5(a) and Fig. 5(c). In this manner, despite the occurrence of velocity drift in radar sensors, it may enhance the odometry calculation being fused with the leg odometry.

#### E. Accurate z-axis Trajectory Estimation

As in Table. II, Radar and Leg calculate precise odometry compared with the comparison group even when used alone. However, Ours shows more accurate odometry results, especially in consequence of the z-axis, which means

**TABLE II:** Experimental result. The evaluation was conducted in terms of ATE translation, ATE rotation, RTE translation, RTE rotation, and ATE on the z-axis. The smallest errors from each sequence are marked in **Bold**.

		EKF-RIO	Mono	Leg	Radar	Ours
Stair	ATE <sub>t</sub>	6.117	6.233	2.024	3.368	<b>1.562</b>
	ATE <sub>r</sub>	4.452	8.672	3.104	3.038	<b>3.022</b>
	RTE <sub>t</sub>	7.110	7.473	4.167	5.037	<b>2.823</b>
	RTE <sub>r</sub>	5.140	5.214	2.668	2.668	<b>2.664</b>
	ATE <sub>z</sub>	5.514	3.572	0.804	1.302	<b>0.717</b>
Under	ATE <sub>t</sub>	8.945	2.343	2.470	2.903	<b>1.685</b>
	ATE <sub>r</sub>	6.972	6.480	<b>1.583</b>	1.635	1.804
	RTE <sub>t</sub>	9.842	4.201	3.478	3.975	<b>2.417</b>
	RTE <sub>r</sub>	7.370	2.814	1.801	1.801	<b>1.791</b>
	ATE <sub>z</sub>	8.336	1.810	2.010	1.802	<b>0.666</b>
Narrow	ATE <sub>t</sub>	2.503	2.884	1.485	0.929	<b>0.757</b>
	ATE <sub>r</sub>	7.585	6.804	2.962	<b>2.708</b>	2.745
	RTE <sub>t</sub>	3.950	3.720	2.483	1.799	<b>1.340</b>
	RTE <sub>r</sub>	7.941	3.873	<b>2.844</b>	<b>2.844</b>	2.845
	ATE <sub>z</sub>	1.264	2.765	0.928	0.339	<b>0.211</b>
Trail	ATE <sub>t</sub>	10.600	6.854	<b>1.943</b>	6.374	2.586
	ATE <sub>r</sub>	14.891	8.167	<b>2.482</b>	2.537	2.485
	RTE <sub>t</sub>	11.757	9.281	<b>3.402</b>	9.665	4.095
	RTE <sub>r</sub>	16.184	4.749	3.044	3.044	<b>3.039</b>
	ATE <sub>z</sub>	2.333	6.314	<b>0.688</b>	2.499	1.068
Garage	ATE <sub>t</sub>	2.519	3.759	<b>1.305</b>	3.108	1.494
	ATE <sub>r</sub>	5.201	6.454	3.968	<b>3.961</b>	4.018
	RTE <sub>t</sub>	2.484	5.065	2.217	4.704	<b>2.137</b>
	RTE <sub>r</sub>	4.940	3.920	2.572	2.572	<b>2.569</b>
	ATE <sub>z</sub>	1.850	3.006	<b>0.575</b>	0.946	0.695
Building	ATE <sub>t</sub>	13.205	7.766	5.215	5.645	<b>4.922</b>
	ATE <sub>r</sub>	16.462	10.737	8.716	<b>8.596</b>	8.781
	RTE <sub>t</sub>	15.361	7.832	6.148	7.005	<b>5.176</b>
	RTE <sub>r</sub>	20.253	10.687	10.516	10.516	<b>10.510</b>
	ATE <sub>z</sub>	7.946	3.944	2.418	2.679	<b>1.167</b>

that the radar and leg odometry factor may work complementarily to increase the precision of the trajectory. Vertical accuracy enhancement by fusing both sensors can be found in Fig. 5(e) and Fig. 5(f). The only sequence that Ours shows a higher error tendency compared with another algorithm is the Trail sequence. As in V-C, this is because consecutive drift occurred in the Radar while Ours is well following the Leg trajectory. Leg operates complementary to the failed Radar, which can be found on both Fig. 5(g) and Fig. 5(j).

#### F. Robust on Vision Failure

One of the key characteristics of our radar factor is that it does not exploit the spatial information to measure the robot's velocity. Similarly, the leg odometry factor utilizes the contact sensor, joint encoder, and angular velocity of IMU, all proprioceptive sensors. Because of this, proposed factors are highly robust on vision failure that might occur on camera or LiDAR. In Fig. 5(c), it can be found that the LiDAR trajectory is not converging to the starting position, which means that scan-matching drift happened on LiDAR because of the narrow path included in the dataset. In contrast, Ours, Radar, Leg show the converging trajectory to the initial position at Fig. 5(c) and Ours generate even accurate results on the z-axis as Fig. 5(f). These findings suggest that the sensor fusion between radar and leg kinematic sensors is highly robust in vision failure environments.

**TABLE III:** Experimental result for radar factor ablation. Error-values refer to ATE<sub>z</sub> (ATE on the z-axis). Results in the first and fourth columns are the same with Mono and Radar in Table. II.

	RANSAC		w/o z-axis outlier reduction	
Optimization	6-DoF	4-DoF	6-DoF	4-DoF
Stair	3.572	3.306	2.384	1.302
Under	1.810	2.030	1.559	1.802
Narrow	2.765	2.293	1.375	0.339
Trail	6.314	6.271	3.684	2.499
Garage	3.006	2.313	1.520	0.946
Building	3.944	4.229	3.063	2.679

S-R, 6-DoF S-R, 4-DoF D-R, 6-DoF D-R, 4-DoF LiDAR

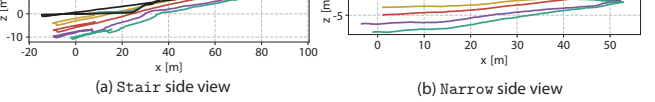


**Fig. 6:** Effects of decoupled RANSAC and 4-DoF optimization to the estimated trajectory. S-R and D-R refer to single or decoupled RANSAC, while 4-DoF and 6-DoF refer to the optimization.

**TABLE IV:** Experimental result for leg factor ablation. Results on the second column are the same with Leg in Table. II.

		w/o rolling contact	with rolling contact
	ATE <sub>t</sub>	ATE <sub>z</sub>	
Stair	12.998	1.610	<b>2.024</b> <b>0.804</b>
Under	3.261	<b>0.671</b>	2.010
Narrow	5.953	<b>0.368</b>	0.928
Trail	2.378	<b>0.611</b>	0.688
Garage	3.541	1.094	<b>1.305</b> <b>0.575</b>
Building	27.094	<b>0.544</b>	5.215 2.418

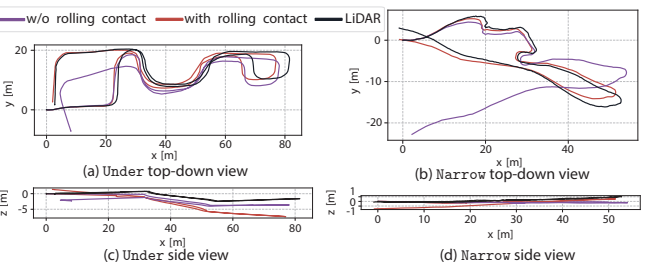


**Fig. 7:** Effect of rolling contact to the estimated trajectory.

#### G. Effects of Decoupled RANSAC & 4-DoF Optimization

Evaluation of the performance of decoupled RANSAC and 4-DoF optimization in section III are done, and results of the experiment are included in Table. III. Outlier reduction using decoupled RANSAC effectively increases z-axis precision compared with the original single RANSAC algorithm, no matter which optimization scheme is utilized. 4-DoF optimization provides higher precision on the z-axis for most cases, but 6-DoF optimization occasionally gives better results when the decoupled RANSAC is not exploited. This concludes that accurate ego-velocity measurement is required to effectively leverage 4-DoF optimization, and decoupled RANSAC performs that role well. Example trajectories about

each combination are included in Fig. 6.

#### H. Effect of Rolling Contact Assumption

The effect of rolling contact assumption in section IV is done, and experiment results are included in Table. IV. Though rolling contact assumption shows a subtle contribution to improving z-axis accuracy, it can be confirmed that it effectively improves overall trajectory precision. This is because, as found from Fig. 3, the rolling contact assumption affects the velocity component on the  $xy$  plane, not in the vertical direction. The significant improvement in horizontal velocity accuracy demonstrates that the rolling contact assumption effectively lowers the burden of leg velocity bias. Example trajectories are included in Fig. 7.

#### I. Computational Cost

Lastly, we compute computational cost analysis for the full system. Since our algorithm leverages sparse radar, contact sensors, and joint encoders, the computational burden is very low. The chip radar we exploited has an sampling rate of 20 Hz, and the proposed system's computational time was 14.21 ms per sequence on average. Time consumption was evaluated on an Intel i7-11700 CPU with 64 GB RAM.

## VI. CONCLUSION

In this paper, we propose two novel factors to generate more precise and robust odometry for the legged robots. By leveraging the additional z-directional noise removal and 4-DoF factor graph optimization scheme, we achieved remarkable performance improvements on radar odometry. Furthermore, based on the rolling contact assumption, we lowered the burden of the bias term in velocity estimation and enhanced the preintegrated odometry factor exploiting the velocity. We evaluated the performance of proposed factors based on the self-collected dataset from various environments, including stairs, slopes, trails, and dynamic objects. The proposed method exhibits robustness and consistent performance even when a single sensor fails, as both sensors work in a complementary manner.

## REFERENCES

- [1] K. Burnett, Y. Wu, D. J. Yoon, A. P. Schoellig, and T. D. Barfoot, “Are we ready for radar to replace lidar in all-weather mapping and localization?” *IEEE Robot. and Automat. Lett.*, vol. 7, no. 4, pp. 10 328–10 335, 2022.
- [2] R. Giubilato, W. Stürzl, A. Wedler, and R. Triebel, “Challenges of slam in extremely unstructured environments: The dlr planetary stereo, solid-state lidar, inertial dataset,” *IEEE Robot. and Automat. Lett.*, vol. 7, no. 4, pp. 8721–8728, 2022.
- [3] Z. Hong, Y. Petillot, and S. Wang, “Radarslam: Radar based large-scale slam in all weathers,” in *Proc. IEEE/RSJ Intl. Conf. on Intell. Robots and Sys.*, 2020, pp. 5164–5170.
- [4] M. Sheeny, E. De Pellegrin, S. Mukherjee, A. Ahrabian, S. Wang, and A. Wallace, “Radiate: A radar dataset for automotive perception in bad weather,” in *Proc. IEEE Intl. Conf. on Robot. and Automat.*, 2021, pp. 1–7.
- [5] C. Zhang, Z. Huang, B. X. L. Tung, M. H. Ang, and D. Rus, “Smart-degradation: A dataset for lidar degradation evaluation in rain,” in *Proc. IEEE/RSJ Intl. Conf. on Intell. Robots and Sys.*, 2023, pp. 7400–7406.
- [6] D. Kellner, M. Barjenbruch, J. Klappstein, J. Dickmann, and K. Dietmayer, “Instantaneous ego-motion estimation using doppler radar,” in *Proc. IEEE Intell. Transport. Sys. Conf.*, 2013, pp. 869–874.
- [7] D. Wisth, M. Camurri, and M. Fallon, “Vilens: Visual, inertial, lidar, and leg odometry for all-terrain legged robots,” *IEEE Trans. Robot.*, vol. 39, no. 1, pp. 309–326, 2022.
- [8] V. Kubelka, M. Vaidis, and F. Pomerleau, “Gravity-constrained point cloud registration,” in *Proc. IEEE/RSJ Intl. Conf. on Intell. Robots and Sys.*, 2022, pp. 4873–4879.
- [9] T. Qin, P. Li, and S. Shen, “Vins-mono: A robust and versatile monocular visual-inertial state estimator,” *IEEE Trans. Robot.*, vol. 34, no. 4, pp. 1004–1020, 2018.
- [10] D. Kellner, M. Barjenbruch, J. Klappstein, J. Dickmann, and K. Dietmayer, “Instantaneous ego-motion estimation using multiple doppler radars,” in *Proc. IEEE Intl. Conf. on Robot. and Automat.*, 2014, pp. 1592–1597.
- [11] C. Doer and G. F. Trommer, “An ekf based approach to radar inertial odometry,” in *Proc. IEEE Intl. Conf. on Multisensor Fusion and Integration for Intell. Sys.*, 2020, pp. 152–159.
- [12] Y. S. Park, Y.-S. Shin, J. Kim, and A. Kim, “3d ego-motion estimation using low-cost mmwave radars via radar velocity factor for pose-graph slam,” *IEEE Robot. and Automat. Lett.*, vol. 6, no. 4, pp. 7691–7698, 2021.
- [13] J. Michalczyk, R. Jung, and S. Weiss, “Tightly-coupled ekf-based radar-inertial odometry,” in *Proc. IEEE/RSJ Intl. Conf. on Intell. Robots and Sys.*, 2022, pp. 12 336–12 343.
- [14] Y. Zhuang, B. Wang, J. Huai, and M. Li, “4d iriom: 4d imaging radar inertial odometry and mapping,” *IEEE Robot. and Automat. Lett.*, 2023.
- [15] H. Chen, Y. Liu, and Y. Cheng, “Drio: Robust radar-inertial odometry in dynamic environments,” *IEEE Robot. and Automat. Lett.*, 2023.
- [16] Q. Huang, Y. Liang, Z. Qiao, S. Shen, and H. Yin, “Less is more: Physical-enhanced radar-inertial odometry,” *arXiv preprint arXiv:2402.02200*, 2024.
- [17] S. Lu, G. Zhuo, L. Xiong, X. Zhu, L. Zheng, Z. He, M. Zhou, X. Lu, and J. Bai, “Efficient deep-learning 4d automotive radar odometry method,” *IEEE Trans. Intell. Vehicles*, 2023.
- [18] R. Hartley, J. Mangelson, L. Gan, M. G. Jadidi, J. M. Walls, R. M. Eustice, and J. W. Grizzle, “Legged robot state-estimation through combined forward kinematic and preintegrated contact factors,” in *Proc. IEEE Intl. Conf. on Robot. and Automat.*, 2018, pp. 4422–4429.
- [19] R. Hartley, M. G. Jadidi, L. Gan, J.-K. Huang, J. W. Grizzle, and R. M. Eustice, “Hybrid contact preintegration for visual-inertial-contact state estimation using factor graphs,” in *Proc. IEEE/RSJ Intl. Conf. on Intell. Robots and Sys.*, 2018, pp. 3783–3790.
- [20] R. Hartley, M. Ghaffari, R. M. Eustice, and J. W. Grizzle, “Contact-aided invariant extended kalman filtering for robot state estimation,” *Intl. J. of Robot. Research*, vol. 39, no. 4, pp. 402–430, 2020.
- [21] D. Wisth, M. Camurri, and M. Fallon, “Preintegrated velocity bias estimation to overcome contact nonlinearities in legged robot odometry,” in *Proc. IEEE Intl. Conf. on Robot. and Automat.*, 2020, pp. 392–398.
- [22] C. Forster, L. Carlone, F. Dellaert, and D. Scaramuzza, “On-manifold preintegration for real-time visual-inertial odometry,” *IEEE Trans. Robot.*, vol. 33, no. 1, pp. 1–21, 2016.
- [23] W. Xu, Y. Cai, D. He, J. Lin, and F. Zhang, “Fast-lio2: Fast direct lidar-inertial odometry,” *IEEE Trans. Robot.*, vol. 38, no. 4, pp. 2053–2073, 2022.
- [24] Z. Zhang and D. Scaramuzza, “A tutorial on quantitative trajectory evaluation for visual(-inertial) odometry,” in *Proc. IEEE/RSJ Intl. Conf. on Intell. Robots and Sys.*, 2018.